



MIT Open Access Articles

Experimental study of the cracking behavior of specimens containing inclusions (under uniaxial compression)

The MIT Faculty has made this article openly available. **Please share** how this access benefits you. Your story matters.

Citation	Janeiro, Raymond, and Herbert Einstein. "Experimental study of the cracking behavior of specimens containing inclusions (under uniaxial compression)." <i>International Journal of Fracture</i> 164.1 (2010): 83-102.
As Published	http://dx.doi.org/10.1007/s10704-010-9457-x
Publisher	Springer
Version	Author's final manuscript
Citable link	http://hdl.handle.net/1721.1/60922
Terms of Use	Attribution-Noncommercial-Share Alike 3.0
Detailed Terms	http://creativecommons.org/licenses/by-nc-sa/3.0/

Experimental Study of the Cracking Behavior of Specimens Containing Inclusions (under Uniaxial Compression)

Raymond P. Janeiro and Herbert H. Einstein

Department of Civil and Environmental Engineering, Massachusetts Institute of Technology, 77 Massachusetts Avenue, Room 1-342, Cambridge, MA 02139, USA

Email: einstein@mit.edu

Abstract: This paper presents the results of an experimental investigation on the cracking behavior of brittle heterogeneous materials. Unconfined, uniaxial compression tests were conducted on prismatic gypsum specimens containing either one, or two, inclusions. These inclusions were of different strengths, stiffnesses, shapes, and sizes. Emphasis was placed on crack coalescence processes associated with specimens containing an inclusion pair, as this was the primary objective of the research. Some observations reported in this study compare well with those of other researchers as the overall cracking sequences are similar. On the other hand, the amount of debonding observed in this study at the inclusion interface is significantly less than what was previously observed. Moreover, the extent of shear crack growth at an inclusion boundary increased substantially in specimens containing two inclusions, compared to those with single inclusions.

Keywords: *inclusions, uniaxial compression, high speed camera, debonding, tensile cracks, shear cracks.*

1. Introduction

The cracking behavior of brittle materials containing inclusions is complicated. It is well known that the strength of a brittle material is governed by the initiation, propagation, and coalescence of cracks during loading. This has been well established experimentally (Griffith 1920; Bombolakis 1963; Brace & Bombolakis 1963; Hoek & Bieniawski 1965; Bieniawski 1967; Nesetova & Lajtai 1973; Horii & Nemat-Nasser 1985 and others) and analytically (Inglis 1913; Griffith 1920; Bienawski 1967; Irwin 1957 and others). Some work has also been done to study cracking in brittle material containing inclusions; specifically, various experimental (Zaitsev and Wittmann 1981; Maji and Shah 1989; 1990; Zhang and Gjørsv 1990;

Aulia 2000 and others) and analytical (Zaitsev and Wittmann 1981; Tasdemir et al. 1989 and others) studies have been performed. Not much work has been done, however, regarding the coalescence of cracks resulting from the presence of inclusions within a material. The underlying question is how the cracking processes in brittle materials occur when there are inclusions. This is of interest for many natural materials (rock) as well as artificial products (concrete and many other composites).

This study aims to broaden the work done by past researchers, specifically understanding, in detail, the crack coalescence processes associated with brittle, composite materials. The purpose of this study was to observe the cracking processes (especially crack coalescence) associated with specimens of gypsum containing inclusions. The research involved uniaxial compression tests on prismatic specimens of gypsum material containing inclusions of various properties (i.e., strength, stiffness, shape, and size). This paper will first present a review of past studies on crack growth within a brittle material containing inclusions (specifically concrete, where much work was done). Then the experimental work performed in this study will be described, including specimen preparation, testing procedure, and results. A comparison of past studies to the present one will subsequently be made, followed by concluding remarks.

2. Previous Studies

The inclusions and matrix of a brittle, heterogeneous material typically have different mechanical properties, specifically the modulus of elasticity, thermal coefficient, and hardening rate (Mitsui et al. 1994). It is, therefore, important to understand if any stress concentrations develop at the interface because of these mechanical differences. If linear elastic behavior is assumed, the property that has the greatest influence on the internal stress distribution of a composite material is the difference between the elastic constants of the inclusion and the surrounding matrix (Hansen 1958; Neville 1997; Aulia 2000 and others). Goodier (1933) derived closed form solutions (which followed those developed by Kirsch (1898)) to predict the stress concentration values

surrounding a spherical particle within a matrix subjected to a far field compressive stress. These solutions will later (in Section 4, “comparison”) be discussed in more detail, since they will help explain the cracking processes observed in this study.

Typically, however, a third phase exists within a heterogeneous material which introduces further variability. This third phase is the interface, or interfacial transition zone, which exists between the matrix and the inclusion and is considered the weakest part of the overall material (Taylor and Broms 1964 and others). The explanation lies within the microstructure of this zone, which is affected by how the matrix and inclusion are produced, either naturally or artificially. In most artificial materials, such as concrete and steel, inclusions (and the imperfections associated with them) are a common result of production. For instance, during casting the particles of a cement paste in concrete are unable to tightly adhere to larger aggregate particles. This is commonly referred to as the *wall effect* as voids form between the paste and aggregate. The result is a very porous interface, which reduces the strength of this zone and, therefore, the strength of the material as a whole (note that while this applies to concrete it does not necessarily apply to other materials). Several visual studies have been performed on concrete in order to observe the interface of inclusions. Zhang and Gjrv (1990) performed SEM analyses on lightweight aggregate interfaces and concluded that as the porosity of the aggregate increased, so did the quality of the bond (Fig. 1b and c). They attributed this to the fact that an increase in porosity improves the mechanical interlock of the aggregate and the matrix. Lo and Cui (2004) confirmed these observations by performing SEM analyses on the interfaces of aggregate with various strengths and also concluded that lightweight aggregate has smaller interface thicknesses compared to normal-weight aggregate.

Several analytical and other experimental studies have also been conducted, specifically on inclusions and their effects within a brittle material. Zaitsev and Wittmann (1981) began modeling the cracking processes of a heterogeneous material by integrating the sliding crack model, which was first introduced by Bombolakis

(1963), into an analysis of a single polygon-shaped inclusion within a matrix subjected to a far field compressive load (Fig. 2). They showed that an inclined interface microcrack will begin to propagate in shear along the interface, but, at the ends of the interface, the same crack will propagate into the matrix in tension (assuming that the tensile strength of the matrix is much lower than its compressive strength). A similar analysis for a matrix containing two polygonal inclusions was also performed. Crack propagation along the interface of a second inclusion was studied assuming a single tensile crack (propagated from the first inclusion) results in the coalescence of the two inclusions (Fig. 3).

Maji and Shah (1989) performed experiments on specimens containing circular inclusions - and void pairs (Fig. 4) and made observations regarding the specimens' cracking and stress/strain behavior. They first created prismatic concrete specimens containing circular, limestone inclusion pairs. Two series of specimens were created containing one-inch and half-inch inclusion pairs. Maji and Shah (1989) reported that interface cracks typically propagated along the entire one-inch limestone inclusion before propagating into the concrete matrix (Fig. 5b). They also noted that interface cracking initiated at various points around the inclusions. This suggests that the interface cracks may not be purely tensile in nature; this is because initiation did not exclusively occur at the right and left inclusion boundary, where tensile stresses perpendicular to the inclusion interface occur (stress concentrations around inclusions are discussed in more detail in Section 4). Just prior to failure, Maji and Shah (1989) observed diagonal cracks, which commonly coalesced with previously initiated vertical matrix cracks (see Fig. 5c). These diagonal cracks typically initiated at the sides of the inclusion boundary, and post-mortem investigations showed that many of these cracks did not extend entirely through the specimen. Regarding the half-inch limestone inclusions, on the other hand, Maji and Shah (1989) reported that no interface and negligible matrix cracking occurred.

Maji and Shah (1989) also created prismatic concrete specimens containing circular, one-inch and half-inch holes. These specimens behaved differently than the

specimens containing inclusions. Matrix cracking always initiated at the top and bottom of the holes, and then propagated in the same fashion as the specimens containing inclusions. These specimens also experienced minor diagonal cracking and failed when spalling of specimen pieces occurred at one of the boundaries.

Tasdemir et al. (1989) extended the principles of mixed-mode fracturing to a crack at a rectangular inclusion interface that refined the work done by Zaitsev and Wittmann (1981). The analytical results were confirmed through experiments in which concrete specimens containing single rectangular inclusions were cast at various inclination angles (Fig. 6). The results showed that the specimens' debonding, initiation, and failure stress decreased as the inclusions' inclination angle increased (where horizontal = 0° and the maximum inclination angle $\approx 72^\circ$). Maji et al. (1991) later performed experiments that verified the analytical work done by Tasdemir et al. (1989) and also showed that the initiation of cracks at a rectangular inclusion interface was not purely tensile, but mixed-mode (tensile behavior dominated, however).

Aulia (2000) performed experiments on concrete specimens where the modulus of elasticity of the matrix (E_m) and aggregate (E_a) were either similar, or very different. When $E_m \ll E_a$ microcracking (which later propagated into the matrix) initiated at the top and bottom of the aggregate interface (i.e., parallel to the direction of compressive load). When $E_m \approx E_a$, on the other hand, microcracking (which later propagated into the matrix) initiated at the sides of the aggregate interface.

To summarize, the experimental and analytical work presented in this section provides a basis for this area of research. The selections of specimen material (especially inclusion shape and strength) were limited, however, due to fabrication issues. In order to thoroughly investigate the main objective of this study (i.e., how crack coalescence is affected by inclusions), specimens containing inclusions of various shapes, sizes, strengths and stiffnesses need to be tested.

3. Experiments

3.1 Specimen Preparation

Unconfined, uniaxial compression tests were conducted on prismatic gypsum specimens containing inclusions. The dimensions of these specimens were 6 inches (height) x 3 inches (width) x 1.25 inches (thickness) (~152mm x ~76mm x ~32mm). As mentioned earlier, inclusion size (one-inch or half-inch), shape (square, circle, hexagon, or diamond), strength, and stiffness were varied. Three gypsum-based materials were used in this study; they are HYDROCAL B-11[®], ULTRACAL[®] 30, and white molding plaster. The inclusions were made of plaster (lower strength and stiffness relative to the Hydrocal matrix) or Ultracal (higher strength and stiffness relative to the Hydrocal matrix). The Hydrocal and Ultracal material are both comprised of calcium sulfate hemihydrate ($\text{CaSO}_4 \cdot 1/2\text{H}_2\text{O}$) and Portland cement, while the molding plaster consists only of hemihydrate. In the laboratory, the gypsum powder is combined with water in order to create hydrated gypsum specimens ($\text{CaSO}_4 \cdot 2\text{H}_2\text{O}$). Table 1 presents the composition and mechanical properties of the three gypsum materials.

The Hydrocal matrices were created using the methods developed by the MIT rock mechanics group (Reyes & Einstein 1991; Shen et al. 1995; Bobet & Einstein 1998; Ko et al. 2006; Wong and Einstein 2009a). To create the Hydrocal paste, HYDROCAL B-11[®] powder, celite powder, and water were combined at a mass ratio of 175:2:70, respectively. After the paste was mixed thoroughly, it was poured into a steel mold. The steel molds used in this study were modified versions of those used by Wong and Einstein (2009a). The mold contained greased nylon bars at different geometries to create the inclusion voids (Fig. 7). Cardboard templates at the top and bottom of the form ensured that the voids were cast at the correct locations within the specimen (see Fig. 8). The specifics of the void (inclusion) geometries will be presented in Sections 3.3 and 3.4.

The hardened specimens were placed in a 40°C oven after their removal from the mold. These specimens were weighed regularly until a constant mass was reached. The specimens were then submerged in a bucket of water prior to pouring the inclusion paste into the voids. To create the paste for a stiff inclusion, ULTRACAL[®] 30 powder and water were combined at a mass ratio of 56:19, respectively. For the less stiff inclusion, molding plaster and water were combined at a mass ratio of 120:81, respectively. The paste was poured into the voids after it was mixed thoroughly. The specimen was then returned to the drying oven until a constant mass was reached. Each specimen was then sanded and dimensioned prior to testing.

Notice that the mechanical properties of the half-inch and one-inch inclusions presented in Table 1 are slightly different. It appears that the half-inch inclusions are somewhat stiffer and stronger than the one-inch inclusions, as a result of the way specimens were cast. The higher values may also be a result of *size effect* (see Baecher and Einstein 1981).

3.2 Experimental Procedure

This section will describe the various components and phases of testing performed in this study. The three main components of the setup were the loading machine, camcorder, and high speed video camera. A schematic of this setup is shown in Fig. 9. The uniaxial compression tests were performed in a Baldwin 200 kip Loading Frame that was controlled by the computer software program MTestW (Version M 9.0.7i) created by ADMET. Load-displacement data were acquired for each of the experiments, which were then synchronized with video recordings in order to obtain a full account of crack initiation, propagation, and coalescence (if the latter is applicable). Load, displacement, and time data were recorded at a rate of 1800 samples per minute.

Real-time and high speed video were captured during each test. A camcorder (Sony DCR-HC65) was used to capture video footage of the specimen surface during each experiment. The camcorder recorded at a rate of thirty frames per second. After

testing, the video footage was converted to a digital format so it could be synchronized with the high speed video footage and stress-strain data. A high speed video (HSV) system (Phantom v7.1) was also used to capture footage of the specimen surface during testing. The primary purpose of the HSV camera was to capture the various cracking processes until failure as well as the crack coalescence sequence (when specimens contained double inclusions). This camera has the capacity of recording up to 30,000 frames per second, but also has a finite amount of memory. Therefore, a lower frame rate had to be used in order to increase the number of frames in the video stream. A frame rate of 5,000 frames per second was chosen as the camera could then capture 1.081 seconds of video. Real-time video was recorded throughout the entire test, while the high speed video was only taken when a significant cracking event occurred. These recordings were used to visually analyze the cracking processes at the specimen's surface. Wong and Einstein (2009b) describe the testing procedures in more detail.

To perform unconfined compression tests, frictional resistance (confinement) at the loaded boundaries needs to be minimized. Many researchers have incorporated various types of media at the boundaries to achieve this goal. The MIT rock mechanics group has been using brush platens (a method also used by others, such as Kupper et al. (1969)). These platens were first developed by Bobet and Einstein (1998) and then redesigned for this study. Fig. 10 shows the details of the platens used here.

3.3 Single Inclusions

The first part of this study examined the cracking sequences associated with specimens containing single inclusions. Four different inclusion geometries (hexagon, square, circle and diamond) were tested to study the effect of inclusion shape on the cracking processes. A total of twenty-four specimens containing one-inch inclusions were tested, and the exact dimensions of these inclusions are shown in Fig. 11. After the single one-inch inclusion series was tested, half-inch circular and square inclusions were then investigated; a total of twelve specimens containing half-

inch inclusions were tested. The main objective was to systematically investigate specimens containing single inclusions (of varying properties) to study crack initiation and propagation; a double inclusion series was later investigated (Section 3.4) using the knowledge obtained from the single inclusion series with the specific objective to observe inclusion interaction effects, notably coalescence.

Fig. 12 and 13 present summaries of typical cracking sequences and relative stress levels for each inclusion size, shape, and material. The relative stress level at each stage was calculated by normalizing the respective stress level when those particular cracks developed, with the maximum stress; this is reported in the top right-hand corner of every image. The ratio of the number of specimens that exhibited the trend to the total number of specimens is reported at the bottom of each image.

The cracking behavior observed in this study can be separated into four categories: interface debonding, tensile cracks, matrix shear cracks, and interface shearing. The difference between *interface debonding* and *interface shearing* is that the former resulted from tensile opening; whereas, the latter resulted from in-plane shearing of the inclusion and matrix boundary. A *matrix shear crack* is defined as shear crack propagation into the specimen matrix.

Summarizing the observations for plaster inclusions, tensile cracks always initiated at a point along the interface first and then propagated into the surrounding matrix. As the load increased, the same tensile cracks typically propagated into the inclusion. For Ultracal inclusions, tensile cracks commonly initiated at a debonded portion of the interface (i.e., the left and right interface boundary) and then propagated into the surrounding matrix; on occasion, tensile cracks initiated within the matrix, just above and below the inclusion. Four basic tensile crack types can be defined as follows (see Fig. 14 and 15):

Type I – Tensile cracks that initiate at the interface and propagate straight,

Type II – Tensile cracks that initiate at the interface and propagate with curvature,

Type III – Tensile cracks that initiate at a pre-test surface crack,

Type IV – Tensile cracks that initiate within the matrix.

In addition to the effects caused by different inclusion materials, the size and shape of an inclusion also had particular effects. Specifically, more debonding was observed as the inclusion size decreased. Debonding occurred at the same locations (i.e., the left and right interface) for both sizes, however (refer to Fig. 12 and 13). Comparison between Fig. 12 and 13 shows that tensile crack initiation was affected by inclusion size, as it typically occurred at lower relative stress levels in specimens containing one-inch inclusions compared to half-inch inclusions. Shape also had an effect on the location of tensile crack initiation. Diamond inclusions, for example, always experienced tensile crack initiation at the upper and lower interface points, regardless of material type (see Fig. 12).

An advantage in using the high speed camera was that not only could the sequence of crack initiation and propagation be captured, but a differentiation between shear and tensile cracks was also possible. As mentioned previously, two types of shearing occurred in addition to tensile cracking: shear crack propagation into the specimen matrix and shearing of the inclusion interface. The location of matrix shear crack initiation depended on inclusion geometry. Such shear cracks typically initiated at the bottom corners of a square inclusion, but always initiated at the centers of the other inclusion shapes (refer to Fig. 12 and 13). Shear cracking also occurred less frequently as the inclusion size decreased. As shown in Fig. 12, the shape of the inclusion seemed to govern the extent of shearing at the inclusion interface, which typically occurred just before specimen failure (i.e., at 99% of maximum stress or later). Shearing at the interface was observed at hexagonal and diamond shaped inclusions, but not at the square or circular inclusions. Regarding the diamond inclusion series, shearing at the interface occurred “simultaneously” with tensile crack initiation (and failure) at the upper and lower interface. The amount of interface shearing typically increased as the inclination of a respective inclusion interface increased. Post-mortem investigations showed that diamond inclusions

completely sheared at the interface (100%), while hexagons experienced moderate shearing (~75%).

The maximum stresses for specimens containing one-inch and half-inch inclusions are shown in Fig. 16. The maximum stresses for the one-inch inclusion geometries varied, with the circular inclusions having the highest average maximum stress. However, unlike what was observed with the one-inch inclusions, the average maximum stress for the half-inch circular inclusions was less than the square inclusions. The average maximum stress for the smaller (half-inch) inclusions was greater than the average maximum stress for the one-inch inclusions, but the increase differed depending on inclusion shape. The specimens containing square inclusions had a stress increase of about fifty percent, while the circular inclusions had an increase of five to twenty percent (see Fig. 16). An explanation for this difference is offered in the following paragraph.

It was observed that pre-test surface cracks within inclusions affected the cracking behavior of specimens. As described in Section 3.1, each specimen was placed into the drying oven after the inclusion paste was poured into the Hydrocal matrix. The inclusion paste lost moisture as it hardened, which resulted in shrinkage cracks. Fig. 17 presents an example of a pre-test surface crack. The occurrence of pre-test surface cracks was more likely in one-inch inclusions compared to half-inch inclusions. They were also common in one-inch square, diamond, and hexagonal inclusions, but not in circular inclusions. The existence of surface cracks may explain why the one-inch inclusions had a lower average maximum stress, and why there is a greater difference between the square and circular maximum stresses of both inclusion sizes. It also appears that pre-test surface cracks had an effect on the tensile crack initiation stress of the specimens, as shown in Table 2.

3.4 Double Inclusions

The second part of this study examined the cracking sequences associated with specimens containing double inclusions. Recall that the major objective of this study

is to determine crack coalescence associated with inclusions, and particularly how these coalescence patterns compare to the patterns observed in different materials containing preexisting cracks but no inclusions. The double inclusions were a half-inch in size, and the shape was either circular or square (Fig. 18). The inclination angle (β) of the inclusion pair was also varied. A total of forty-two specimens were tested, and a summary of typical coalescence patterns for each specimen's geometry is presented in Fig. 19 and 20, and Tables 3 and 4. The number at the top right-hand corner of each image represents the coalescence category after Wong and Einstein (2009a) (which are shown in Fig. 21), while the fraction at the bottom right-hand corner represents the number of specimens showing that particular behavior out of the number of specimens tested.

Typically, the tensile cracking processes associated with the double inclusion series were very similar to the single inclusion series. The four tensile crack types discussed in Section 3.3 were again observed in this series (see Fig. 14 and 15). One of these tensile crack types always initiated first, which was later followed by the initiation of matrix shear cracks at the inclusion boundary. The propagation of these shear cracks into the matrix resulted in the coalescence of the inclusion pair (either exclusively or in combination with tensile cracks, as described next). An example of a typical cracking sequence for specimens containing an inclusion pair is shown in Fig. 22 (refer to Fig. 19 and 20, and Tables 3 and 4 for specific details regarding each geometry).

In many cases, the initiation of primary tensile cracks had some effect on coalescence. This effect was either *direct* (when the coalescence involved a primary crack) or *possible* (when the coalescing crack initiated at the same inclusion as primary tensile crack initiation). Typically, a *direct* effect on coalescence only occurred for the circular $\beta = 60^\circ$ series and the square $\beta = 75^\circ$ series. *Possible* effects on coalescence were common in all other series.

A complex relationship exists between the maximum stresses of both circular and square inclusion pairs (Fig. 23 and 24). Specimens containing plaster inclusions typically had a higher maximum stress and tensile crack initiation stress (see Fig. 25 and 26) compared to specimens containing Ultracal inclusions. As mentioned previously, this is possibly a result of pre-test surface cracks located especially within Ultracal inclusions. For example, all three specimens in the Ultracal, circular $\beta = 30^\circ$ series contained pre-test surface cracks, while the other two series ($\beta = 0^\circ$ & 60°) only had one specimen containing visible pre-test surface cracks. This may explain the drop in maximum stress shown in Fig. 23. Also, all of the specimens in the circular $\beta = 0^\circ$ plaster series contained pre-test surface cracks, which may explain the lower relative maximum stresses compared to the other plaster series in Fig. 23. Regarding the square series, eleven out of twelve Ultracal specimens contained visible pre-test surface cracks, while only three out of the twelve plaster specimens contained surface cracks. Further investigation into the effects of surface cracks is still needed, however.

A major difference between the double inclusion series and the single inclusion series was the significance of shear crack initiation at the inclusion interface and propagation into the matrix. For specimens containing single inclusions, shear crack propagation was a *randomly* occurring effect. The extent and direction of shear crack propagation differed even with specimens of the same type. With the double inclusion series, however, shear crack initiation and propagation was common and consistent among specific geometries. Specifically, it was typical that all specimens of a particular geometric series coalesced in the same way (see Fig. 19 and 20).

4. Comparison of this Study to Others

In this comparison section, emphasis will be placed on the occurrence of interface debonding, tensile and shear cracking, and most importantly, coalescence. Debonding (prior to tensile crack propagation into the matrix) was found to be minor in all cases of this study, but was slightly more extensive at the interfaces of half-inch inclusions compared to the one-inch inclusions. When debonding initiated in this

study, it typically occurred only at the right and left inclusion boundaries. Other researchers such as Maji and Shah (1989), Tasdemir et al. (1989), and Maji et al. (1991) all observed complete interface debonding prior to tensile crack initiation, however. The difference might be attributable to the difference in the mechanical properties of materials between this study and others, along with specimen preparation methods, but additional experimental work needs to be performed to clarify this point. Moreover, a microscopic analysis (such as the ones performed by Zhang and Gjørsv (1990), and Lo and Cui (2004)) may contribute to better understanding this phenomenon.

Stress distributions were calculated in an attempt to explain the observed cracking processes (specifically debonding and tensile crack initiation) for inclusions of different strengths and stiffnesses. The results of these closed formed solutions tend to agree with the results observed in this study. Fig. 27 shows the stress concentration factors associated with a hole ($E = 0$) and a rigid inclusion ($E = \infty$) set in an infinite plate subject to a vertical far field uniaxial, compressive stress. Both the tangential stress (σ_θ) and radial stress (σ_r) concentration factors are plotted. It is assumed that the Poisson's ratio (ν) of the plate is 0.25.

According to Fig. 27, the matrix containing a hole experiences high tangential compressive stresses ($\sigma_c = 3\sigma_o$) at the right and left interface, and moderate tensile stresses ($\sigma_t = -\sigma_o$) at the top and bottom interface. Transition into a compressive stress then occurs further above and below the hole. The matrix containing a rigid inclusion experiences different stress concentrations. The top and bottom interface experiences compressive tangential stresses ($\sigma_c \approx 0.38\sigma_o$), but a transition into tensile stresses then occurs at about a distance of half the inclusion's radius from the interface. Both the radial and tangential stresses are also plotted for the sides of the rigid inclusion. Note that the tangential stresses are compressive, while the radial stresses are tensile.

These closed form solutions can be compared to the cracking behavior observed in this study. Fig. 28 compares the cracking patterns for the Ultracal, circular inclusions to the “rigid inclusion” model shown in Fig. 27. As mentioned earlier, debonding (prior to tensile crack propagation into the matrix) only occurred at the sides of the inclusion interface. This agrees with the presence of tensile radial stresses at the sides of the rigid inclusion model. Since the tensile strength of gypsum is about a tenth of its compressive strength, tensile debonding is likely to initiate first. It was also observed that tensile crack initiation occurred in the matrix above and below the inclusion (as shown in Fig. 28a) in some specimens containing half-inch, Ultracal inclusions. The plot in Fig. 28c agrees with this observation as tensile tangential stresses occur just above and below the inclusion.

The tendency for tensile crack initiation at the upper and lower interface of plaster inclusions (Fig. 29a) can be explained through comparison to the hole model in Fig. 27. According to the closed form solutions, the tangential tensile stresses at these locations are relatively high. Again, since the tensile strength of a typical gypsum material is about a tenth of its compressive strength, it is likely that tensile cracks should initiate at the top or bottom of the interface. This can also explain why tensile cracks initiated at plaster inclusions at lower stresses compared to the Ultracal inclusions, since a higher tensile stress concentration exists just above and below the plaster inclusion compared to the rigid (Ultracal) inclusion model.

Interestingly, these closed form solutions (along with the observations from this study) do not agree with the tensile crack initiation results reported by Aulia (2000), but appear to agree with the work done by Maji and Shah (1989). Aulia (2000) stated that when large differences between E_m and E_a exist, as in the case of a high-strength concrete ($E_m \ll E_a$), microcracking will occur at the top and bottom interface. He also stated that when the differences between E_m and E_a are small, microcracking will occur at the sides of the interface. Aulia (2000) did not provide sound reasoning to back up his theory, other than the fact that the theory agreed with his experimental work. This discrepancy could be caused by the fact that Aulia (2000) did not test

specimens containing single inclusions, but concrete specimens containing numerous inclusions. The experimental work performed by Maji and Shah (1989) appears to agree to some extent with the tensile crack initiation predictions from the closed form solutions, considering that they reported that the entire inclusion typically debonded prior to tensile crack propagation into the matrix. If one assumes that complete debonding may make the inclusion correspond to the hole model rather than the stiff inclusion model, it might explain why in their experiments tensile crack initiation commonly occurred at the top and bottom of the debonded interfaces.

The initiation of shear cracks (that propagated into the matrix) at an inclusion boundary was not reported by any other researcher prior to this study. Here the propagation of shear cracks was a common phenomenon that resulted in the coalescence of all specimens containing inclusion pairs. As mentioned earlier, Maji and Shah (1989) frequently observed the initiation of “diagonal” cracks at the sides of the inclusion interface. They did not, however, report the nature (tensile/shear) of these diagonal cracks. Based on the results of this study, these diagonal cracks may have been shear cracks. The occurrence of surface spalling was commonly observed in this study adjacent to a propagating matrix shear crack, which would explain Maji and Shah’s (1989) post-mortem observations regarding diagonal cracks not extending through the entire specimen.

The other type of shear cracking (interface shearing) can also be compared to other studies. In this study, interface shearing typically initiated at the inclined boundary of hexagon and diamond inclusions. The results from Zaitsev and Wittmann (1981) and Tasdemir et al. (1989) essentially agree with these observations. Zaitsev and Wittman (1981) attributed this phenomenon to the presence of stresses on the inclined interface, and used it as a fundamental assumption for their analytical work. Comparison can also be made with the work done by Tasdemir et al. (1989) on specimens containing an inclined rectangular inclusion. The present study consisted of a square and diamond inclusion series, where the diamond inclusions had an interface inclination angle of 45° and the square inclusions had an interface

inclination angle of 0° . As shown in Fig. 16, the average failure stress for the one-inch, diamond inclusion series was lower than the square series (regardless of inclusion material), which is consistent with the results of Tasdemir et al. (1989).

Regarding specimens containing two inclusions, the coalescence patterns observed in this study can be compared to the results of Wong and Einstein (2009a) for specimens containing a flaw pair (i.e., existing cracks). The results of this study match those reported by Wong and Einstein (2009a) quite well (see Fig. 30). For example, the horizontal inclusion pair (square and circle) and the horizontal, coplanar flaw pair geometries reported by Wong and Einstein (2009a) both coalesced indirectly along two or more cracks. The experimental series performed by Maji and Shah (1989) on horizontal inclusion pairs also agrees with the results from this study, as both studies observed that the horizontal inclusion pair typically coalesced indirectly (Fig. 5, 19 and 20). The results of the analytical study by Zaitsev and Wittman (1981) can also be related to this study (refer to Fig. 3). As mentioned earlier, Zaitsev and Wittman (1981) assumed that coalescence only occurred along a single tensile crack for an overlapping inclusion pair. In this study, however, coalescence never occurred through a single tensile crack; this may be explained by the fact that no specimens containing overlapping inclusions were tested in this study. In some specimens where the inclusion inclination angle was large (i.e., close to overlapping), however, the propagation of tensile cracks (along with propagating matrix shear cracks) resulted in coalescence. Fig. 31 presents a visual comparison of the coalescence patterns observed by Zaitsev and Wittman (1981), Wong and Einstein (2009a), and this study. To fully confirm the similarities, it will be necessary to test specimens containing overlapping inclusion geometries.

5. Conclusions

Many advances have been made in studying the cracking behavior associated with material containing inclusions. This study consisted of an experimental series that considered the effects of inclusion shape, size, stiffness, and strength on the cracking behavior of materials containing inclusions. While past work consisted of

experimental and analytical studies with the same intentions, none have systematically studied crack coalescence resulting from inclusion interaction.

In this study, the first objective was to obtain an idea on the cracking behavior of specimens containing a single inclusion of four different shapes (hexagon, square, circle and diamond) and two different sizes (one-inch and half-inch). The series showed that tensile and shear cracks can be distinguished, each in the form of interface cracking (i.e., tensile debonding and shearing) or tensile and shear cracks within the matrix. The type of cracking varied with inclusion characteristics, specifically size, shape, stiffness, and strength. Tensile debonding and tensile cracking within the matrix compared well to theoretical solutions, in which tensile stresses occur at different locations and in different magnitudes depending on the relative stiffness of the inclusion and matrix. Tensile cracking for single inclusions was also affected by size, as it initiated at lower stress levels (relative to the maximum stress) for the larger inclusions compared to the smaller inclusions. Shear cracking occurred for all shapes when the inclusions were large but only rarely for the smaller ones. Although the location of shear cracking varied, it always occurred at the lateral extremities of the inclusions. These experimental observations and theoretical considerations (where applicable) regarding tensile cracks around single inclusions correspond well to those of other researchers. It appears, however, that no other research so far has reported shear cracking. This is probably due to the fact that the high speed video system used in this study made it possible to distinguish the cracking processes.

The single inclusion experiments in this study are interesting but are subsidiary to the major objective, namely, the study of crack coalescence in conjunction with inclusion pairs. For this purpose, square and circular shaped half-inch inclusions of different stiffnesses, cast at various inclination angles, were investigated. The major result was that crack coalescence, which eventually leads to failure, always involved shear cracking or shear cracks coalescing with tensile cracks. The tensile cracks (when they occurred) were analogous to those observed for single inclusions, attesting to the

necessity of the preceding experimental series. Very relevant in this regard is the fact that the observed crack coalescence patterns with inclusion pairs can be compared to crack coalescence behavior of specimens containing pre-existing cracks. Extensive testing on crack coalescence between pre-existing cracks (so-called flaws) of different sizes and inclinations had been conducted by the same research group. The results observed with the inclusion pairs compared well to those with pre-existing cracks. There is also reasonable correspondence to the few experimental and analytical results obtained by others.

The systematic study of the effect of single and, particularly, of double inclusions on crack and crack-coalescence behavior showed results, which confirm those of similar studies. Additionally, the study revealed behavior that had not been observed previously. This indicates that continued experimentation along the lines of what has been reported is necessary in order to eventually provide the basis for analytical modeling.

Acknowledgments: This study was sponsored by the National Science Foundation Geomechanics and Geotechnical Systems Program under Grant CMMI-0555053. The authors would like to thank the National Science Foundation for their continued support in this research topic.

References

- Aulia, T.B. (2000) Strain localization and fracture energy of high-strength concrete under uniaxial compression. *LACER* 5: 221-240
- Baecher, G.B.; Einstein, H.H. (1981) Size effect in rock testing. *Geophys Res Lett*, 8(7): 671–674
- Bienawski, Z.T. (1967) Mechanisms of brittle fracture of rock, part II – experimental studies. *Int J Rock Mech Min Sci* 4: 407-423
- Bobet, A.; Einstein, H.H. (1998) Fracture coalescence in rock-type materials under uniaxial and biaxial compression. *Int J Rock Mech Min Sci* 35(7): 863-88
- Bombolakis. (1963) Photoelastic stress analysis of crack propagation within a compressive stress field. Ph.D. Thesis, Massachusetts Institute of Technology, Cambridge: 38p
- Brace, W.F.; Bombolakis, E.G. (1963) A note on brittle crack growth in compression. *J Geophys Res* 68(12): 3709-3713
- Goodier, J.N. (1933) Concentration of stress around spherical and cylindrical inclusions and flaws. *J Appl Mech* 1: 39-44

- Griffith, A.A. (1920) The phenomenon of rupture and flow in solids. *Phil Trans A221*: 163-198
- Hansen, T.C. (1958) Creep of Concrete. *Swed Cem Conc Res Inst* 33: 48p
- Hoek, E.; Bieniawski, Z.T. (1965) Brittle fracture propagation in rock under compression. *Int J Frac Mech* 1: 137-155
- Horii, H.; Nemat-Nasser, S. (1985) Brittle failure in compression: splitting, faulting, and brittle-ductile transition. *Phil Trans A319*: 337-374
- Inglis, C.E. (1913) Stresses in a plate due to the presence of cracks and sharp corners. *Inst Naval Arch* 55: 219-230
- Irwin, G.R. (1957) Analysis of stresses and strains near the end of a crack traversing a plate. *J of App Mech* 24: 361-364
- Kirsch, G. (1898) Die Theorie der Elastizitat und die Bedurfnisse der Festigkeitslehre. *Zeitschrift des Vereines Deutscher Ingenieure* 42: 797-802
- Ko, T.Y.; Einstein, H.H.; Kemeny, J. (2006) Crack coalescence in brittle material under cyclic loading. *Proc 41st U.S. Symp on Rock Mech (USRMS)*. Golden, Colorado, ARMA/USRMS 06-930
- Kupfer H.; Hilsdorf H.K.; Rusch, H. (1969) Behavior of concrete under biaxial stresses. *ACI J, Proceedings* 66(8): 656-666
- Lo, T.Y.; Cui, H.Z. (2004) Effect of porous lightweight aggregate on strength of concrete. *Mat Lett* 58: 916-919
- Maji, A.K.; Shah, S.P. (1989) Application of acoustic emission and laser holography to study microfracture in concrete. In: Lew, H.S. (ed) *Nondestructive Testing*, ACI SP-112. American Concrete Institute, Detroit, MI: 83-109
- Maji, A.K.; Shah, S.P. (1990) Mixed mode fracture in compression. In: Elfgrén, L. and Shah, S.P. (ed) *Analysis of Concrete Structures by Fracture Mechanics*. Chapman and Hall, New York, NY: 55-68
- Maji, A.K.; Tasdemir, M.A.; Shah, S.P. (1991) Mixed mode crack propagation in quasi brittle material. *Eng Frac Mech* 38(2/3): 1058-107
- Mitsui, K.; Li, Z.; Lange, D.A.; Shah, S.P. (1994) Relationship between microstructure and mechanical properties of the paste-aggregate interface. *ACI Mat J* 91(1): 30-39
- Nesetova, V.; Lajtai, E.Z. (1973) Fracture from compressive stress concentrations around elastic flaws. *Int J Rock Mech Min Sci* 10:265-284
- Neville, A.M. (1997) Aggregate bond and modulus of elasticity of concrete. *ACI Mat J* 94(1): 71-74
- Reyes, O.; Einstein, H.H. (1991) Failure mechanism of fractured rock – a fracture coalescence model. In: Wittke, W. (ed) *Proc 7th Int Cong of Rock Mech*. Aachen, Germany: 333-340
- Shen, B.; Stephansson, O.; Einstein, H.H.; Ghahreman, B. (1995) Coalescence of fractures under shear stress experiments. *J Geophys Res* 100(6): 5975-90
- Tasdemir, M.A.; Maji, A.K.; Shah, S.P. (1989) Crack propagation in concrete under compression. *J Eng Mech* 116(5): 1058-1076

- Taylor, M.A.; Brooms, B.B. (1964) Shear bond strength between coarse aggregate and cement paste or mortar. *Proc ACI J* 61(8): 937-957
- Wong, L.N.Y.; Einstein, H.H. (2009a) Crack coalescence in molded gypsum and Carrara marble: part 2—microscopic observations and interpretation. *Rock Mech and Rock Eng* 42: 475-511
- Wong, L.N.Y.; Einstein, H.H. (2009b) Using high speed video imaging in the study of cracking processes in rock. *Geo Test J* 32(2): 164-180
- Zaitsev, Y.B.; Wittmann, F.H. (1981) Simulation of crack propagation and failure of concrete. *Mat Struc* 14(83): 357-365
- Zhang, M.H.; Gjrv, O.E. (1990) Microstructure of the interfacial zone between lightweight aggregate and cement paste. *Cem Conc Res* 20(4): 610-618

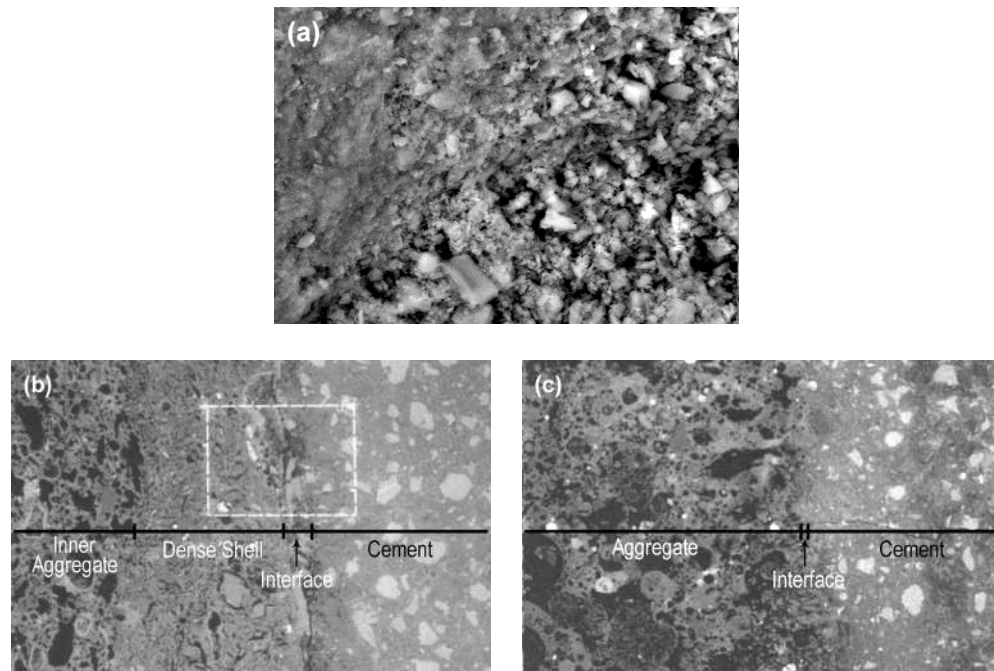


Figure 1. (a) An ESEM image showing the porous interfacial transition zone of a stiff inclusion (top left) from this study and its surrounding gypsum matrix (bottom right) at a 2500x magnification, (b) A SEM image detailing a piece of aggregate with a dense outer shell at a 200x magnification (Zhang and Gjrv 1990), (c) A SEM image detailing a porous aggregate piece with no outer shell at a 200x magnification (Zhang and Gjrv 1990).

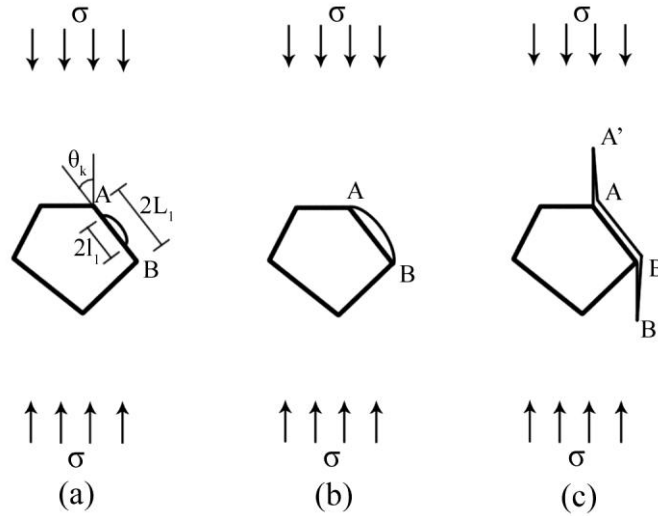


Figure 2. Application of Sliding Crack Model to Interface Cracks - Tensile crack of length, $2l_1$, is located at the inclusion interface, AB: (a) initial crack, (b) propagation of the crack along the inclusion face, (c) propagation of the crack into the surrounding matrix (Zaitsev and Wittmann 1981).

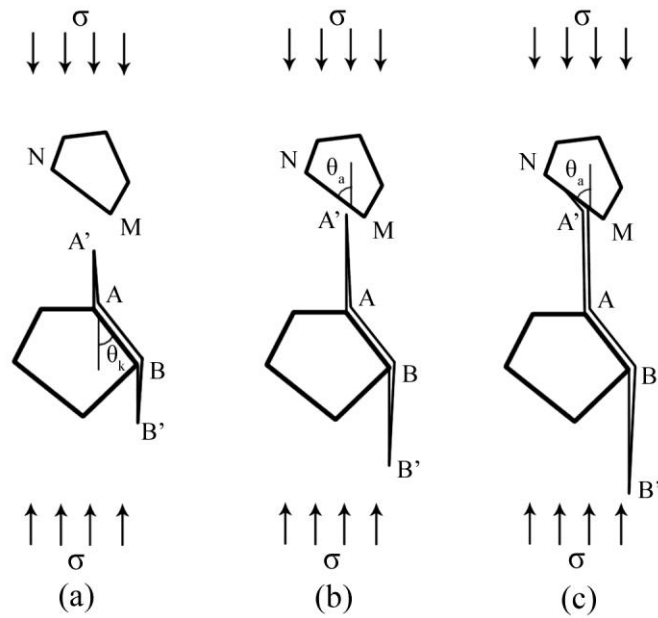


Figure 3. Extension of Fig. 2 with more than one inclusion: (a) initial crack presented in Fig. 2c, (b) propagation of the crack until its coalescence with the second inclusion, (c) propagation of the crack along the boundary of the second inclusion (Zaitsev and Wittmann 1981).

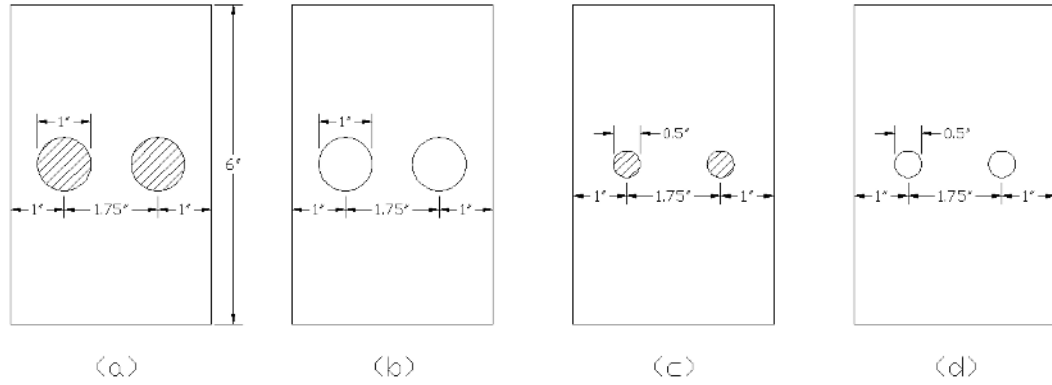


Figure 4. Specimen geometries tested by Maji and Shah (1989): (a) 1" diameter limestone inclusion; (b) 1" diameter hole; (c) 1/2" diameter limestone inclusion; (d) 1/2" diameter hole.

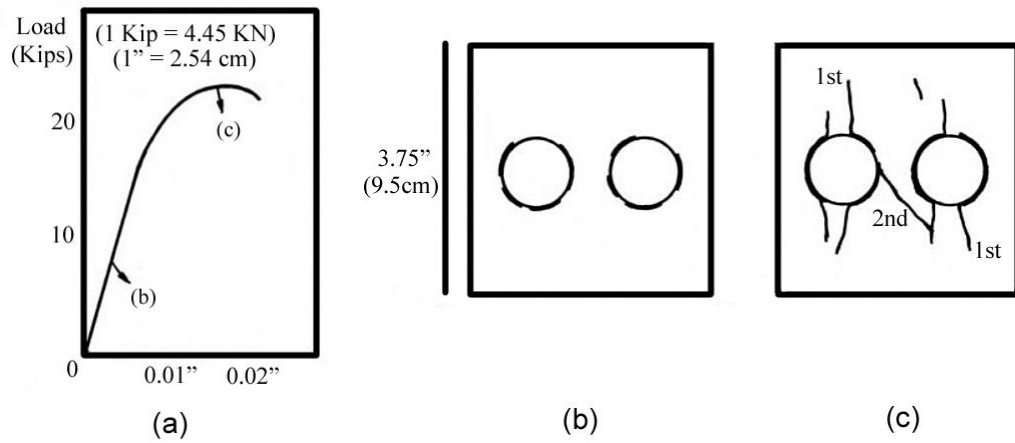


Figure 5. (a) Load-displacement diagram for a 1" diameter limestone specimen (b) sketch of bond (interface) crack initiation, (c) sketch of specimen just prior to failure (Maji and Shah 1989).

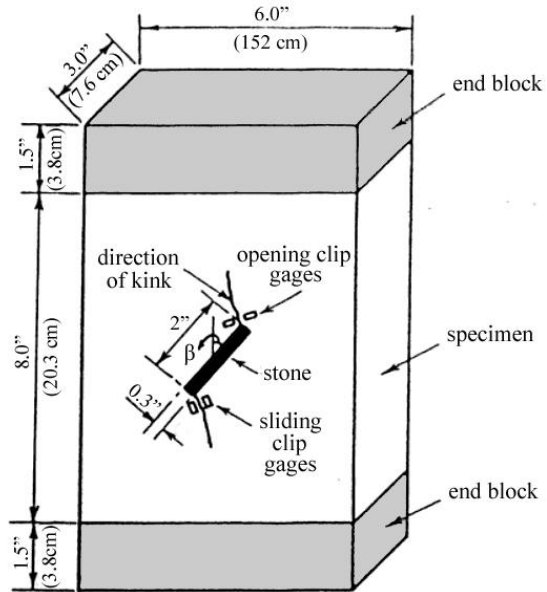


Figure 6. Geometry of a specimen containing a rectangular limestone inclusion (labeled as “stone”) cast at an inclination angle β (Maji and Shah 1989).

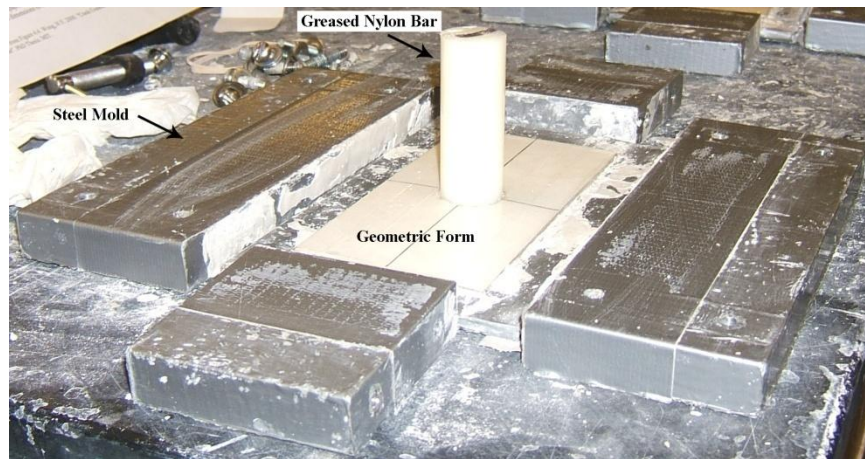


Figure 7. Steel mold used to cast specimens containing a greased nylon bar set within a cardboard geometric form.

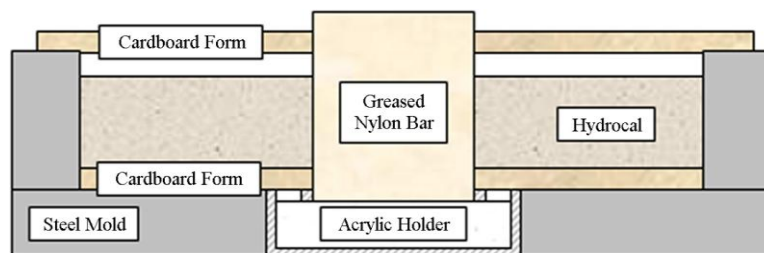


Figure 8. Cross-section of a specimen within the steel mold.

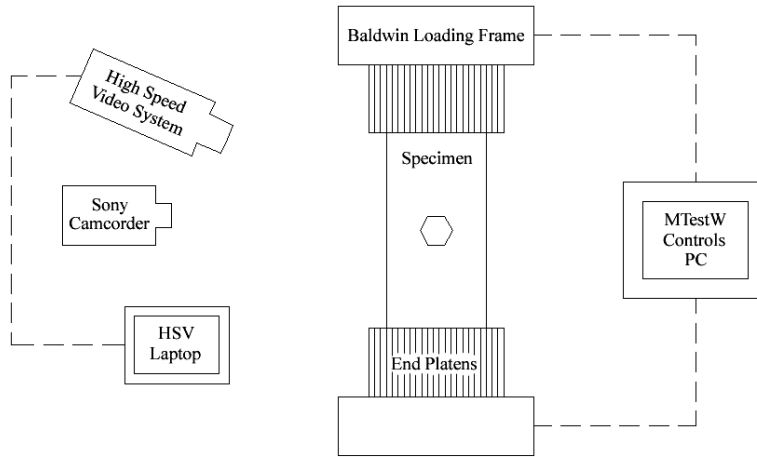
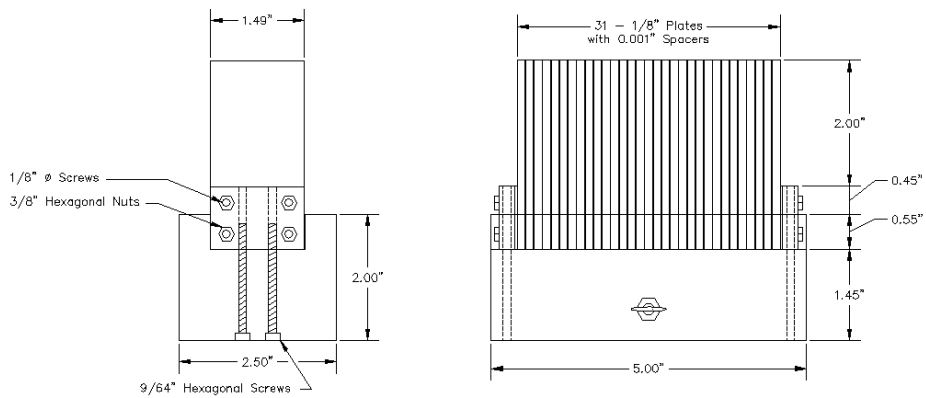


Figure 9. Schematic of a typical experimental setup.



All materials made of A36 Steel

Figure 10. End platens used in the current study.

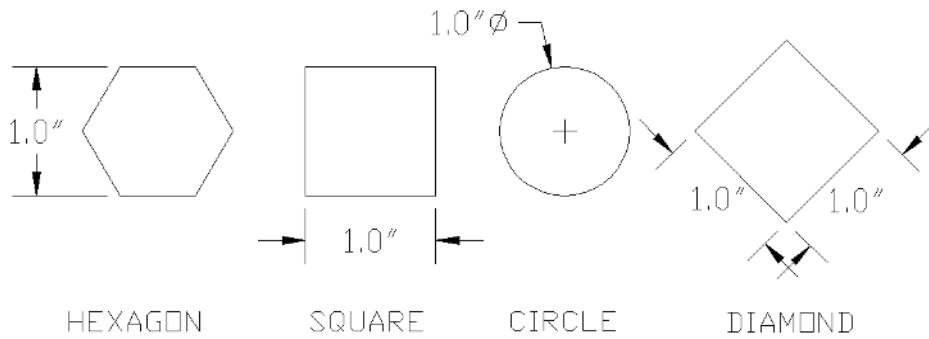


Figure 11. Four inclusion geometries used in the specimens containing one-inch single inclusions.

1" Inclusion Shape & Material		Initial Geometry	Typical Fracturing Sequence and Relative Stress Levels		
Circle	Plaster		(71%) 3/3	(83%) 3/3	(98%) 2/3
	Ultracal		(94%) 2/3	(97%) 2/3	(99%) 3/3
Hexagon	Plaster		(63%) 3/3	(83%) 3/3	(99%) 3/3
	Ultracal	(2/3) Pre-test Surface Crack	(81%) 3/3	(89%) 3/3	(99%) 3/3
Diamond	Plaster		(82%) 3/3	(92%) 2/3	(94%) 3/3
	Ultracal		(99%) 3/3	(99%) 2/3	(99%+) 3/3
Square	Plaster		(67%) 2/3	(75%) 2/3	(93%) 2/3
	Ultracal	(3/3) Pre-test Surface Crack	(65%) 2/3	(69%) 1/3 one side 1/3 both sides	(92%) 1/3 one side 1/3 both sides

Figure 12. Crack sequences for the single, one-inch inclusions, where T = tensile cracks, (T) = tensile debonding, S = shear cracks, and (S) = interface shearing. The number at the top right-hand corner of

each image is the relative stress level at each stage shown, while the fraction in the bottom represents the number of specimens showing that particular behavior out of the number of specimens tested.

1/2" Inclusion Shape & Material		Initial Geometry	Typical Fracturing Sequence and Relative Stress Levels		
Circle	Plaster		 T (94%) T 2/3	 T (95%) T 2/3	 T (98%) S S T 3/3
	Ultracal		 (T) (90%) (T) 2/3	 T (93%) (T) T (T) 2/3	 T (95%) (T) S S (T) T 3/3
Square	Plaster		 (T) (99%+) 2/3	 T (99%+) (T) T 3/3	 T (99%+) (T) T 3/3
	Ultracal		 (T) (94%) (T) 2/3 one side 1/3 both sides	 T (95%) (T) T (T) 2/3 one side 1/3 both sides	 T (99%+) (T) T (T) 2/3 one side 1/3 both sides

Figure 13. Crack sequences for the single, half-inch inclusions, where T = tensile cracks, (T) = tensile debonding, and S = shear cracks. The number at the top right-hand corner of each image is the relative stress level at each stage shown, while the fraction in the bottom represents the number of specimens showing that particular behavior out of the number of specimens tested.

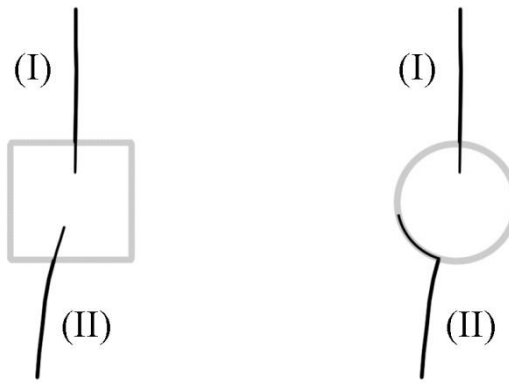


Figure 14. Typical tensile crack initiation and propagation at a square (left) and circle (right) plaster inclusion.

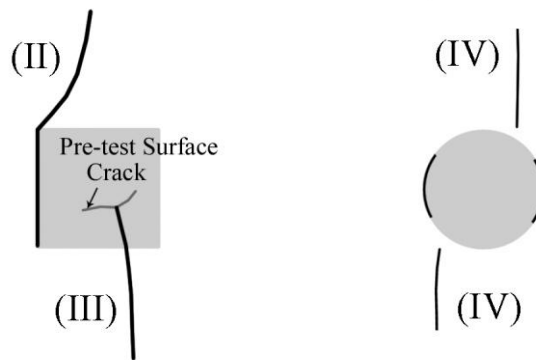


Figure 15. Typical tensile crack initiation and propagation at a square (left) and circle (right) Ultracal inclusion. Note the pre-test surface crack located within square inclusion (refer to Section 3.3)

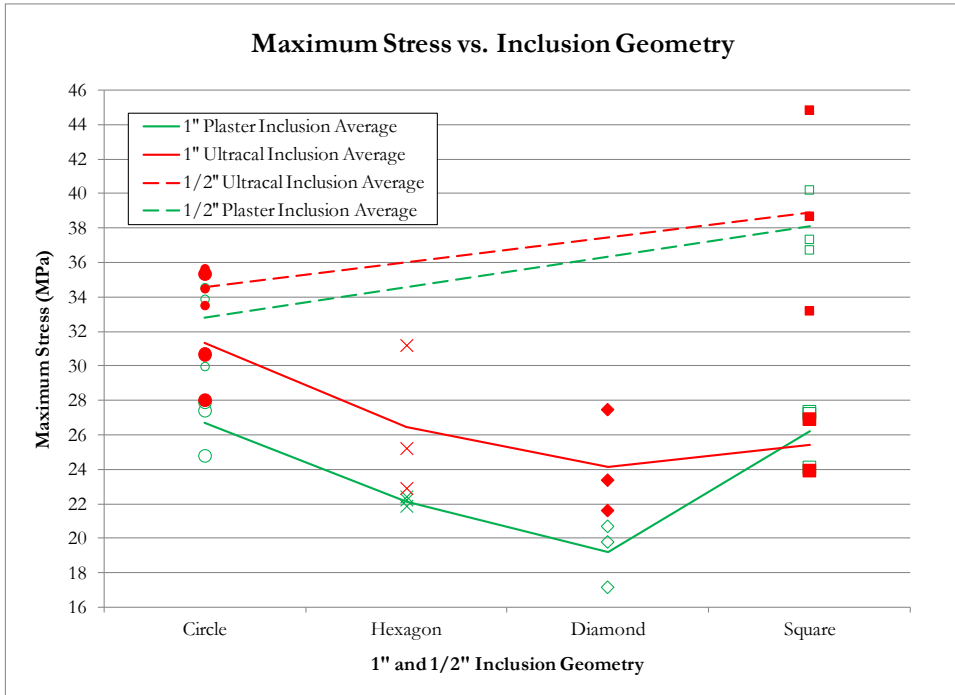


Figure 16. Maximum stresses for specimens with one-inch and half-inch, single inclusions. The solid points represent the values for the Ultracal inclusions, while the hollow points represent the values for the plaster inclusions. The lines connect the averages for each geometry and material type.

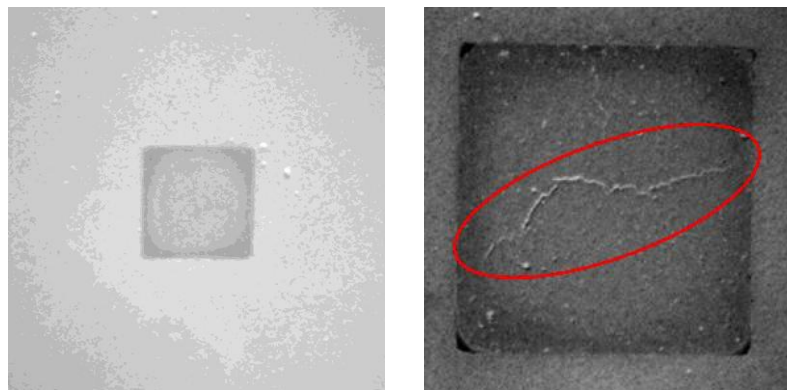


Figure 17. Half-inch square inclusion showing no visible pre-test surface cracks (left) and a one-inch square inclusion containing a distinct pre-test surface crack (right).

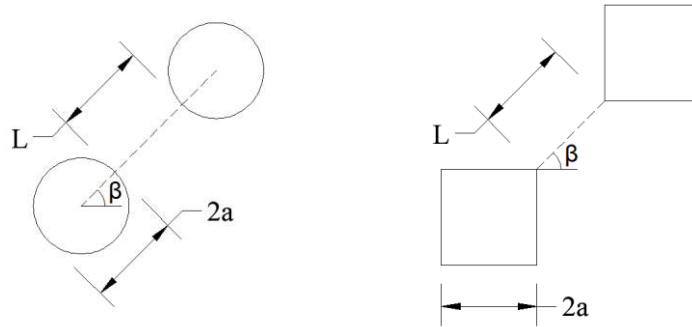


Figure 18. Double inclusion geometries for the square and circle half-inch inclusions, showing also inclination angle (β) and a ligament length (L).

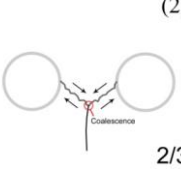
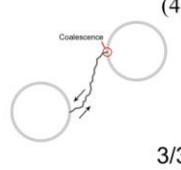
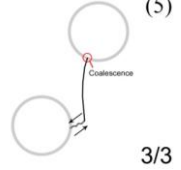
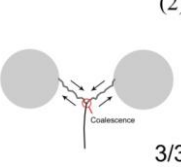
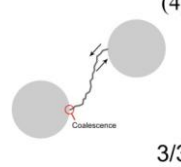
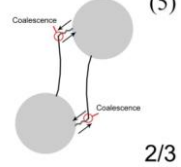
Circle Inclusion	Inclination Angle (β)		
	$\beta = 0^\circ$	$\beta = 30^\circ$	$\beta = 60^\circ$
Plaster	 (2) 2/3	 (4) 3/3	 (5) 3/3
Ultracal	 (2) 3/3	 (4) 3/3	 (5) 2/3

Figure 19. Coalescence patterns for the circular inclusion pair series. The number in parenthesis represents the coalescence category observed (refer to Figure 21), while the fraction represents the number of specimens showing that particular behavior out of the number of specimens tested.

Square Inclusion	Inclination Angle (β)			
	$\beta = -45^\circ$	$\beta = 30^\circ$	$\beta = 60^\circ$	$\beta = 75^\circ$
Plaster				
Ultracal				

Figure 20. Coalescence patterns for the square inclusion pair series. The number in parenthesis represents the coalescence category observed, while the fraction represents the number of specimens showing that particular behavior out of the number of specimens tested.

Category	Coalescence patterns	Crack types involved
1		No coalescence
2		Indirect coalescence by two or multiple cracks (crack types vary)
3		Type 2 S crack(s)
4		Type 1 S crack(s)
5		One or more type 2 S crack(s) and type 2 T crack segments between inner flaw tips
6		Type 2 T crack(s). There may be occasional short S segments present along the coalescence crack.
7		Type 1 T crack(s)
8		Flaw tips at the same side linked up by T crack(s) not displaying wing appearance (crack type not classified). There may be occasional short S segments present along the coalescence crack.
9		Type 3 T crack(s) linking right tip of the top flaw and left tip of the bottom flaw. There may be occasional short S segments present along the coalescence crack.

Figure 21. The nine coalescence patterns reported by Wong and Einstein (2009a), where T = tensile cracks and S = shear cracks.

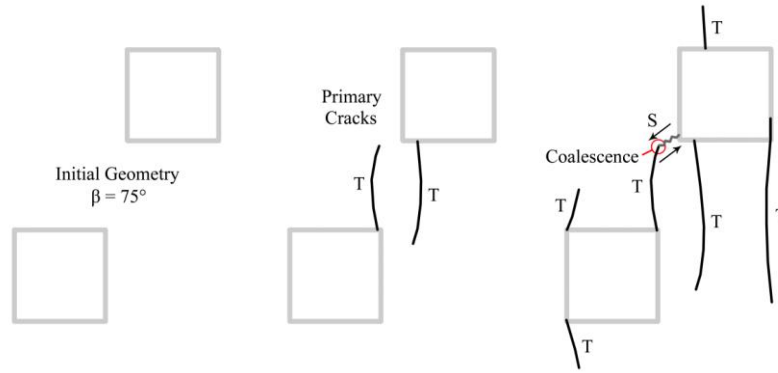


Figure 22. Typical cracking sequence for specimens containing inclusion pairs, where T = tensile and S = shear. Refer to Fig. 19 and 20, and Tables 3 and 4 for specific details regarding each geometry.

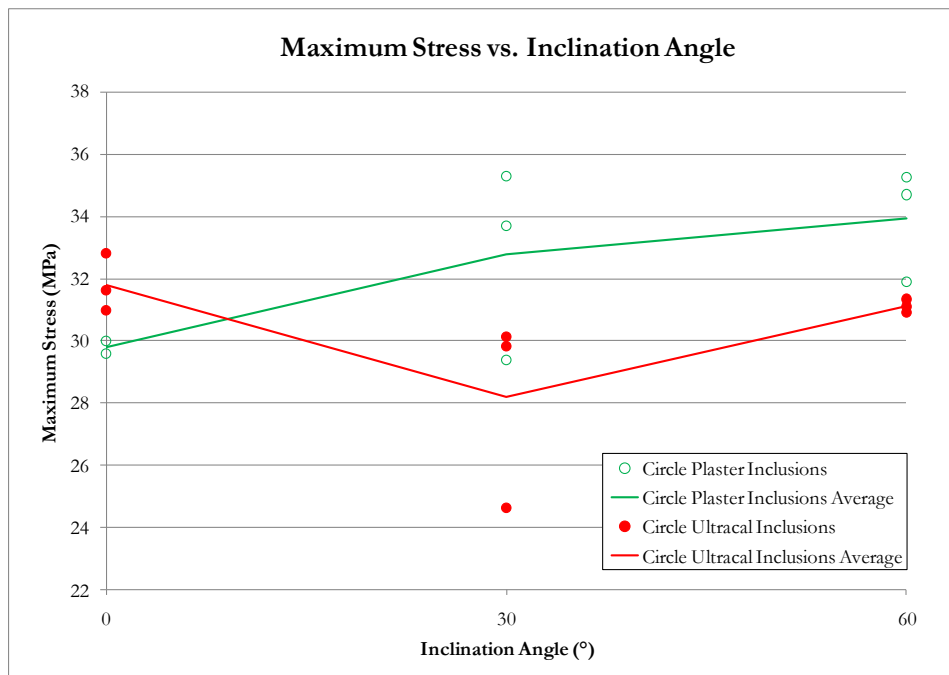


Figure 23. Maximum stresses for the circular, double inclusion series. The solid points represent the values for the Ultracal inclusions, while the hollow points represent the values for the plaster inclusions. The lines connect the averages for each inclination angle and material type.

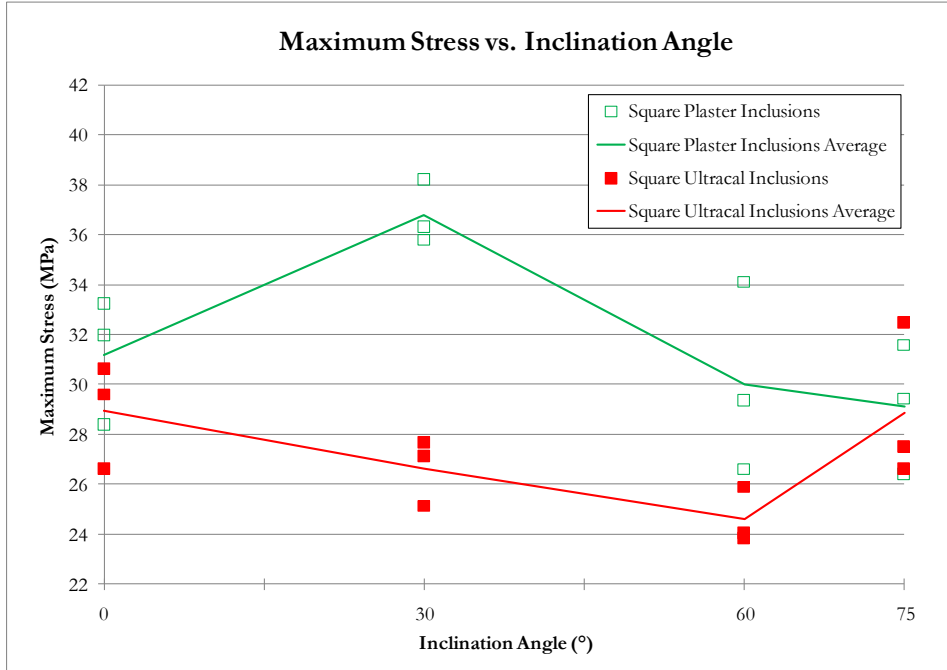


Figure 24. Maximum stresses for the square, double inclusion series. The solid points represent the values for the Ultracal inclusions, while the hollow points represent the values for the plaster inclusions. The lines connect the averages for each inclination angle and material type.

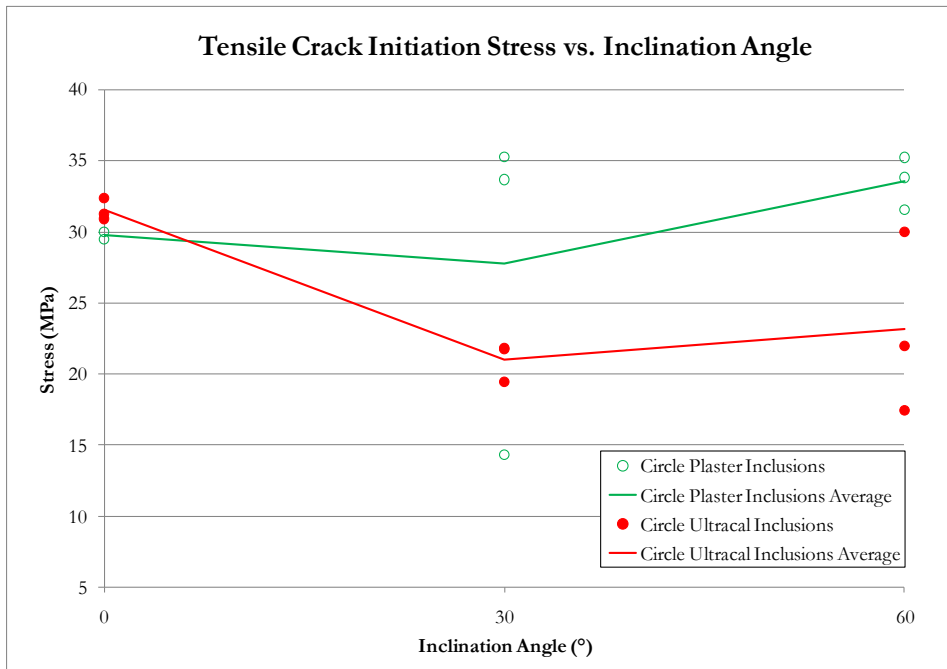


Figure 25. Tensile crack initiation stresses for the circular, double inclusion series. The solid points represent the values for the Ultracal inclusions, while the hollow points represent the values for the plaster inclusions. The lines connect the averages for each inclination angle and material type.

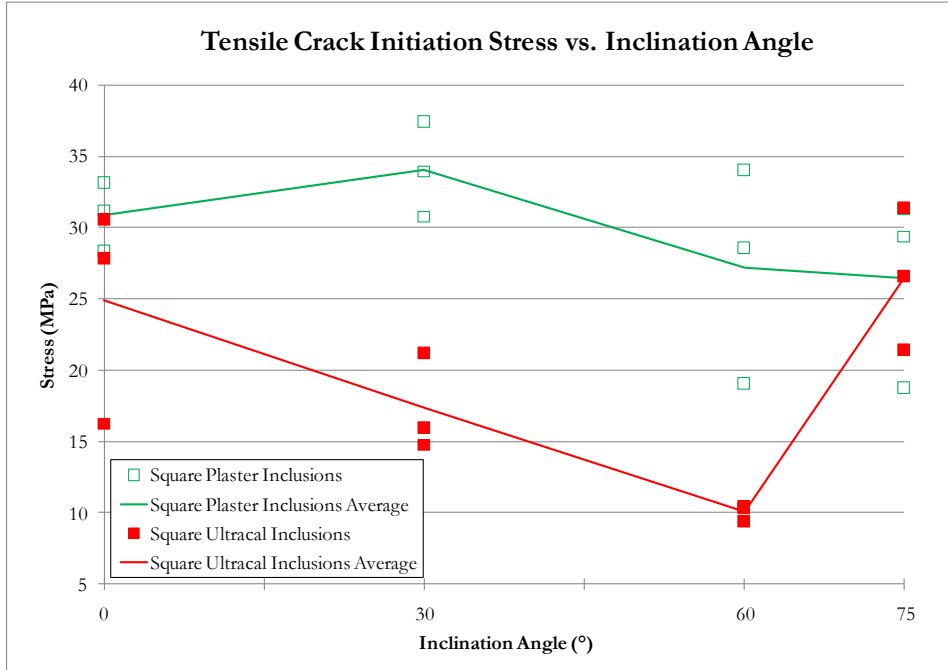


Figure 26. Tensile crack initiation stresses for the square, double inclusion series. The solid points represent the values for the Ultracal inclusions, while the hollow points represent the values for the plaster inclusions. The lines connect the averages for each inclination angle and material type.

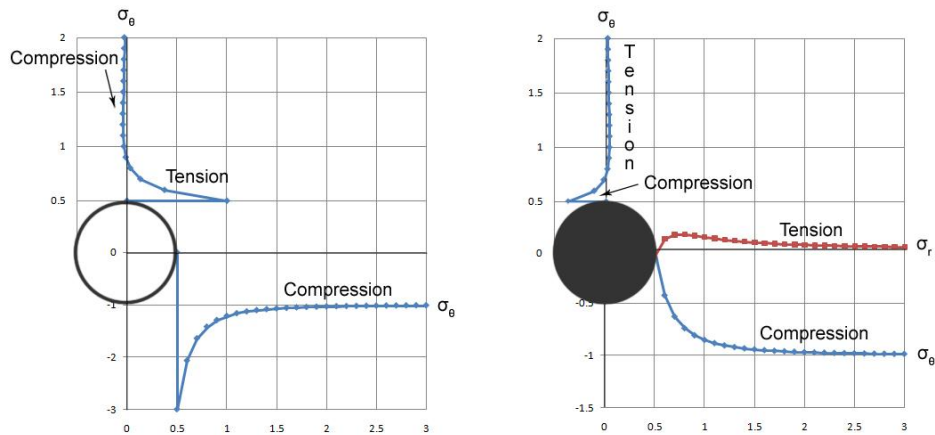


Figure 27. Plots showing the tangential (σ_t) and radial (σ_r) stress concentration factors for a hole (left) and a rigid inclusion (right) cast within an infinite plate (for $\nu = 0.25$) subject to a far field uniaxial compressive stress (σ_0) in the vertical direction.

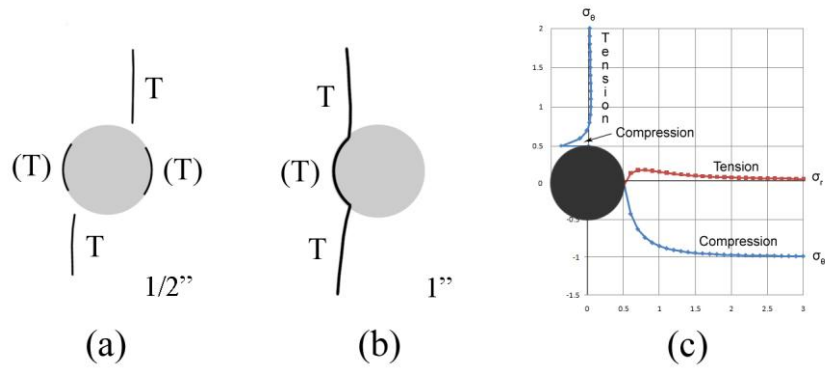


Figure 28. Comparison of the one-inch (a) and half-inch (b) Ultracal, circular inclusions to the plot (c) showing the tangential (σ_t) and radial (σ_r) stress concentration factors for the rigid inclusion in Fig. 27.

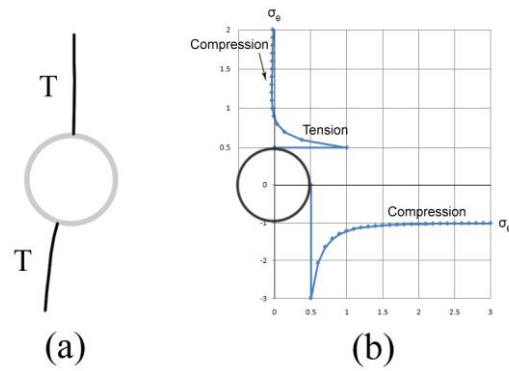


Figure 29. Comparison of the plaster, circular inclusions (a) to the plot (b) showing the tangential (σ_t) stress concentration factors for the model containing a hole in Fig. 27.

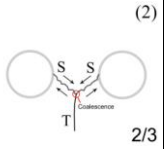
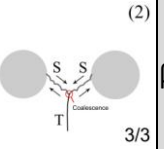
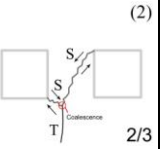
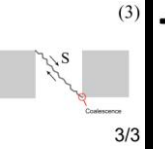
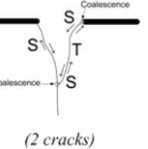
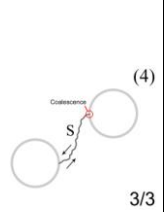
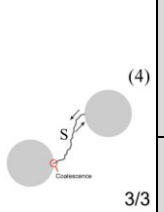

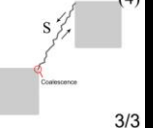


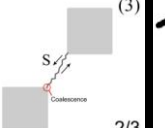
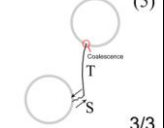
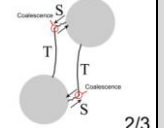


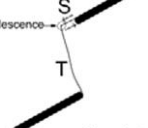
	PLASTER INCLUSIONS	ULTRACAL INCLUSIONS		PLASTER INCLUSIONS	ULTRACAL INCLUSIONS	Wong & Einstein (2009a)
$\beta = 0^\circ$	 (2) 2/3	 (2) 3/3	$\beta = -45^\circ$	 (2) 2/3	 (3) 3/3	 (2 cracks)
$\beta = 30^\circ$	 (4) 3/3	 (4) 3/3	$\beta = 30^\circ$	 (4) 1/3 (2/3 no coal.)	 (4) 3/3	 (1 crack)
			$\beta = 60^\circ$	 (3) 1/3 (1/3 no coal.)	 (3) 2/3	
$\beta = 60^\circ$	 (5) 3/3	 (5) 2/3	$\beta = 75^\circ$	 (5) 2/3	 (5) 2/3	 (2 cracks)

Figure 30. Sketch of the double inclusion coalescence patterns from this study, compared to the $\beta=0^\circ$, $\beta=30^\circ$, and $\alpha=60^\circ$ ($\beta=30^\circ$) geometries (where α = bridging angle of flaw pair) reported by Wong and Einstein (2009a). The fraction represents the number of specimens showing that particular behavior out of the number of specimens tested.

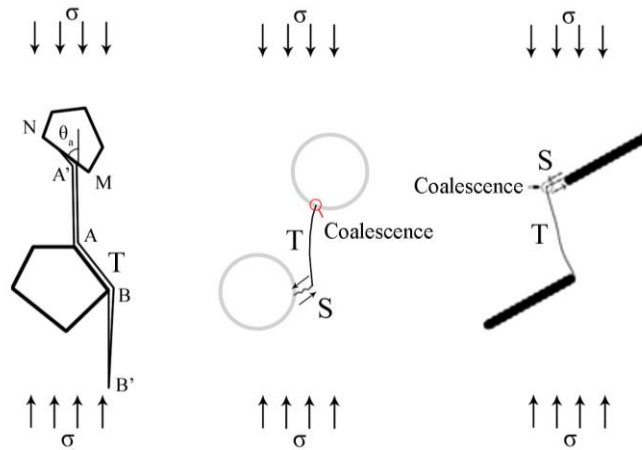


Figure 31. Comparison of the coalescence patterns observed by Zaitsev and Wittmann (1981) (left), this study (center), and Wong and Einstein (2009a) (right).

Table 1. Composition and mechanical properties of the three gypsum materials.

Material Properties	Material				
	Hydrocal [®]	Plaster		Ultracal [®]	
		½" Size	1" Size	½" Size	1" Size
CaSO ₄ · ½H ₂ O (wt%)	>85	100		>85	
Portland Cement (wt%)	<10	0		<10	
Crystalline Silica (wt%)	<5	<1		<5	
Density, ρ [g/cm ³]	1.55	1.33	1.32	2.11	2.09
Young's Modulus, E [GPa]	15.0	10.5	9.29	29.0	28.1
Compressive Strength, σ _c [Mpa]	37.20	28.55	27.55	91.10	86.92

Table 2. Comparison of average tensile crack initiation ratios (i.e., tensile crack initiation stress divided by the maximum stress) between one-inch inclusions containing surface cracks, versus no visible surface cracks. Note the differences in the Ultracal, hexagon inclusion series and the plaster, diamond inclusion series.

		Circle	Hexagon	Diamond	Square
1" Inclusion	Plaster w/ surf. cracks	N/A	62.9%	62.6%	N/A
	Plaster w/o surf. cracks	70.9%	N/A	92.1%	66.7%
	Ultracal w/ surf. cracks	N/A	81.3%	N/A	64.9%
	Ultracal w/o surf. cracks	93.7%	99.9%	99.9%	N/A

Table 3. Summary of cracking behavior for the circular inclusion pairs. Numbers in parentheses represent the number of specimens that experienced that behavior compared to the total number of specimens tested.

* A *possible* effect on coalescence is when the initiation of the first shear crack occurred at the same inclusion as primary tensile crack initiation, while a *direct* effect is when coalescence involved primary tensile cracks.

** First crack initiated at the lower loaded specimen boundary and propagated towards an inclusion.

	Inclination Angle	First (Primary) Cracks To Appear	*Effect of Primary Cracks on Coalescence	Coalescence Cracks
Plaster Inclusions	$\beta = 0^\circ$	Type II (2/3)	Possible (2/3)	Category 2 (2/3) No Coalescence (1/3)
	$\beta = 30^\circ$	Type II (2/3)	Possible (1/3) None (2/3)	Category 4 (3/3)
	$\beta = 60^\circ$	Type II (3/3)	Direct (3/3)	Category 5 (3/3) – two cracks
Ultracal Inclusions	$\beta = 0^\circ$	Type II (3/3)	Possible (2/3) None (1/3)	Category 2 (3/3)
	$\beta = 30^\circ$	Type I (1/3) Type III (1/3) Type IV (1/3)	Possible (3/3)	Category 4 (3/3)
	$\beta = 60^\circ$	Type II (1/3) Boundary** (2/3)	Direct (3/3)	Category 5 (1/3) – two cracks Category 5 (2/3) – four cracks

Table 4. Summary of cracking behavior for the square inclusion pair series. Numbers in parentheses represent the number of specimens that experienced that trait compared to the number of specimens tested.

	Inclination Angle	First (Primary) Cracks To Appear	Effect of Primary Cracks on Coalescence	Coalescence Cracks
Plaster Inclusions	$\beta = 0^\circ$	Type I (2/3) Type II (1/3) Type IV (1/3)	Possible (2/3)	Category 2 (2/3) No Coalescence (1/3)
	$\beta = 30^\circ$	Type I (3/3)	Possible (1/3)	Category 4 (1/3) No Coalescence (2/3)
	$\beta = 60^\circ$	Type I (2/3) Type III (1/3)	Direct (1/3) None (1/3)	Category 3 (1/3) Category 4 (1/3) No Coalescence (1/3)
	$\beta = 75^\circ$	Type II (2/3) Type III (1/3)	Direct (2/3)	Category 5 (2/3) – two cracks No Coalescence (1/3)
Ultracal Inclusions	$\beta = 0^\circ$	Type II (1/3) Type III (1/3) Type IV (1/3)	Possible (3/3)	Category 3 (3/3)
	$\beta = 30^\circ$	Type I (1/3) Type II (1/3) Type III (1/3)	Possible (2/3) None (1/3)	Category 4 (3/3)
	$\beta = 60^\circ$	Type II (2/3) Type III (1/3)	Possible (3/3)	Category 3 (2/3) Category 4 (1/3)
	$\beta = 75^\circ$	Type II (1/3) Type III (1/3) Type IV (1/3)	Direct (2/3)	Category 5 (2/3) – two cracks No Coalescence (1/3)